Mode locking in a periodically forced resonate-and-fire neuron model

Azadeh Khajeh Alijani*
Mathematics Institute, University of Warwick, Coventry CV4 7AL, United Kingdom
(Received 21 May 2009; revised manuscript received 3 October 2009; published 25 November 2009)

The resonate-and-fire (RF) model is a spiking neuron model which from a dynamical systems perspective is a piecewise smooth system (impact oscillator). We analyze the response of the RF neuron oscillator to periodic stimuli by expressing the firing events in terms of an implicit one-dimensional time map. Based on such a firing map, we describe mode-locked solutions and their stability, leading to the so-called Arnol'd tongues. The boundaries of these tongues correspond to either local bifurcations of the firing time map or grazing bifurcations of the discontinuity of the flow. Despite the fact that the periodically driven RF system shows periodic firing, its behavior may become chaotic when the forcing frequency is near the resonant frequency. We compare these results to numerical simulations of the model undergoing sinusoidal forcing. Furthermore, upon varying a system parameter, the RF system can be reduced to the integrate-and-fire system and in this case we show the consistency of the results on mode-locked solutions.

DOI: 10.1103/PhysRevE.80.051922 PACS number(s): 87.19.ln, 05.45.−a

I. INTRODUCTION

Biological neurons exhibit a wide range of ionic conductances in their soma and dendrites. These different currents are responsible for action potential generation and may also lead to complex dynamics including bursting, periodic oscillations, etc. Of particular interest are the creation of resonance and subthreshold damped oscillations as a result of interaction between specific currents. The resonant behavior, in which the response of the induced oscillating voltage peaks at a preferred input frequency, has been observed in many biological neurons, for example, in thalamic [1,2], cortical neurons [3–5], hippocampal CA1 pyramidal cells [6], and interneurons [7]. It is known that receptor cells in auditory and electroreceptive systems of many species show electrical resonance; also in amphibian cochlea, hair cells behave like small electrical resonant elements [8]. The resonant and oscillatory behavior is also believed to play an important role in brain activities, e.g., the possible functional importance of resonance and oscillations observed in thalamic and cortical neurons lies in the known participation of these neurons in various brain rhythms. The low-frequency resonances in the cortex and thalamus appear suited to support the thalamocortical delta wave oscillations which are particularly prominent during deep sleep. The higher-frequency oscillatory behavior and underlying resonance in pyramidal and inhibitory neurons of the neocortex might have some involvement with higher-frequency rhythms that appear in the cortex during cognition [9].

To understand these nontrivial ideas, neurodynamical models based on spiking neurons are used. They play an increasing role in the interpretation of neurophysiological data [10]. Importantly, we are interested in studying the precise timing of firing events that is thought to underly several different forms of sensory processing [11]. We use the resonate-and-fire (RF) neuron model to explore the effects of periodic forcing on the firing dynamics of the resonant neurons. Analyzing the response of neurons to periodic forcing has long been investigated [12,13]. Also many interesting neuron models have been previously used to analyze the response of spiking neurons to periodic stimuli [10,14–21]. Among them, the integrate-and-fire (IF) models and the modified IF models are of particular interest, as they are the simplest spiking neuron models capable of reproducing a great deal of known features of real neurons. For example, the periodically forced leaky integrate-and-fire model reproduces rectification and phase-locking behavior [22–24] and can display quasiperiodic and periodic firing trains [10], integrate-and-fire-or-burst reproduces temporal tuning of both post-inhibitory rebound bursting and tonic spiking [16], the ghostbursting model can exhibit chaotic bursting [20], and the integrate-and-fire model with threshold fatigue [15] can exhibit chaotic behavior. However, these simple models fail to generate subthreshold damped oscillations and resonance that have been observed in certain neurons [4,25] and in almost all biophysically detailed Hodgkin-Huxley (HH)-type neuron models [4,9]. This motivated the introduction of the RF model [26–28] (called the generalized integrate-and-fire model in [26,28]) to describe more accurately these types of subthreshold properties.

The RF model is the simplest possible model to exhibit subthreshold resonance. It has piecewise smooth dynamics such that the effect of the flow reaching threshold is to cause an instantaneous jump in the flow, so that a complete description in terms of smooth differential equations is no longer possible. This kind of dynamics is described in the context of impact oscillators or more generally of hybrid systems [29].

The effect of resonance on the firing properties of the neurons has been investigated in [26,28]. It is found that a sufficient level of noise is necessary for the subthreshold resonance to be seen in the firing rate modulation and when noise is weak, the firing rate response is amplified at the background firing frequency. However, we show here that even in the absence of noise, the subthreshold resonance is revealed such that the firing times show chaotic behavior near the resonant frequency. In this paper, our approach for a periodically driven RF system, similar to that in [10,20], is

*azadeh.khajeh-alijani@warwick.ac.uk

based on firing map formulation, analyzing the mode-locked solutions, and constructing their instability borders in parameter space leading to the Arnol'd tongues structure. A dynamical systems approach also allows us to go further and classify periodically forced RF dynamics as periodic, quasiperiodic, and chaotic. It is believed that variability in the firing times of periodically forced neurons is not necessarily due to noise but could be also due to chaotic behavior [30,31]. Using the Liapunov exponent notion, we show here that the RF system can exhibit chaotic behavior.

The outline of the paper is as follows. In Secs. II and III, we introduce the RF neuron model by applying the linearization theory of Koch [8] for the HH equations with just one ionic current. In Secs. III A and III B, the periodically forced RF system is considered such that the effect of the flow crossing threshold is to cause both voltage and current to be reset. We can express the firing times of the RF model in the form of an implicit one-dimensional time map and can describe mode-locked solutions by formulating a set of nonlinear simultaneous equations that any mode-locked solutions must satisfy. Then we continue in Sec. III C by treating the stability of these solutions which can be affected by smooth and nonsmooth bifurcations and show our numerical results on the Arnol'd tongues. In Sec. IV, using the idea of impact oscillators [32], we are able to derive an expression for the largest Liapunov exponents of the RF system. We will show that the system can move from periodic to chaotic behavior (positive Liapunov exponent) as the forcing frequency is close to the resonant frequency. Finally, in Sec. V, we discuss the results of this paper and suggest some extensions of our work.

II. LINEARIZED VOLTAGE-DEPENDENT CURRENTS

It is a well-known fact that a small excitatory synaptic input in the presence of voltage-dependent channels will lead to a local depolarization, followed by hyperpolarization. Such an overshooting response indicates the presence of the so-called *RLC* circuits which include resistances, capacitances, as well as inductances [8]. Although a real neuron does not have any elements such as inductance, neuron membranes within certain types of voltage and time-dependent conductances can behave as if they contained inductances [8] . This phenomenological inductance was first described by Cole [33,34] in the squid axon. We use the Koch theory [8,35] to explain how an inductancelike behavior can arise from a membrane by linearizing the HH equations.

In order to demonstrate the principle behind this linearization, let us consider the HH equation in which the dynamics of membrane voltage satisfies

$$c\dot{v} = -g_L(v - v_L) - \sum_{k=1}^{M} I_k + I_{app}(t), \tag{1}$$

where c is the physical capacitance of the bilipid membrane, g_L is the leakage conductance, v_L is leakage reversal potential, I_{app} is the applied current, and I_k's are ionic currents. Instead of the total ionic current in Eq. (1), we consider a

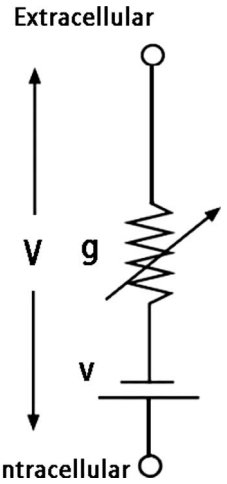

FIG. 1. Equivalent electrical circuit for voltage gated current I with nonlinear conductance g and reversal potential v.

generic current $I(v, n_1, \ldots, n_M)$ as a function of membrane voltage and M gating variables $(n_1, \ldots, n_M)$. The equivalent electrical circuit of the current I with nonlinear conductance g is shown in Fig. 1. The conductance is shown with an arrow to indicate that it can vary with the membrane voltage. The gating variables n_k's satisfy

$$\frac{d}{dt}n_k = \alpha_k(v)(1 - n_k) - \beta_k(v)n_k, \quad k = 1, \ldots, M, \tag{2}$$

where α_k and β_k are voltage-dependent rates. Now consider small variations of the ionic current I around some fixed point. We can express such a variation as

$$\delta I = \left(\frac{\partial I}{\partial v}\right)_{ss} \delta v + \sum_{k=1}^{M} \left(\frac{\partial I}{\partial n_k}\right)_{ss} \delta n_k, \tag{3}$$

where subscript ss denotes that derivatives are evaluated at the equilibrium point. Retaining only the first-order terms, we expand Eq. (2) for a small variation into the following form:

$$\frac{d}{dt}(\delta n_k) = \delta\alpha_k - (\delta\alpha_k + \delta\beta_k)n_k - (\alpha_k + \beta_k)\delta n_k. \tag{4}$$

Since both α_k and β_k are only dependent on the membrane potential, their variations can be expressed as

$$\delta\alpha_k = \left(\frac{d\alpha_k}{dv}\right)\delta v, \quad \delta\beta_k = \left(\frac{d\beta_k}{dv}\right)\delta v. \tag{5}$$

Substituting Eq. (5) into Eq. (4) leads to

$$\frac{d}{dt}(\delta n_k) = \left(\frac{d\alpha_k}{dv}\right)\delta v - (\alpha_k + \beta_k)\delta n_k - n_k\left(\frac{d(\alpha_k + \beta_k)}{dv}\right)\delta v. \tag{6}$$

This can be formally written as

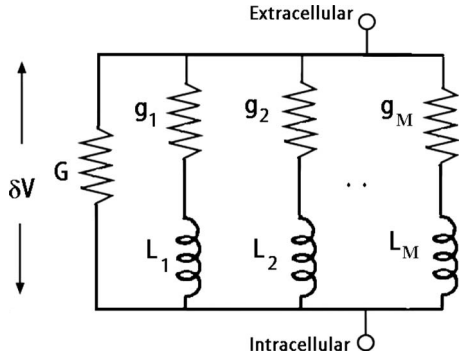

FIG. 2. Electrical circuit when ionic current $I(v,n_1,\ldots,n_M)$ of Fig. 1 is linearized around the equilibrium point.

$$\left(\frac{d}{dt}+\alpha_k+\beta_k\right)\delta n_k=\left[\left(\frac{d\alpha_k}{dv}\right)-n_k\left(\frac{d(\alpha_k+\beta_k)}{dv}\right)\right]\delta v. \quad (7)$$

After substituting this result into Eq. (3), we get the following equation for the first order of variation of current I:

$$\delta I=\left[G+\sum_{k=1}^{M}\frac{a_k}{\frac{d}{dt}+b_k}\right]\delta v, \quad (8)$$

where $G=(\frac{\partial I}{\partial v})_{ss}$. Two parameters a_k and b_k need to be evaluated at the steady state such that

$$a_k=\left(\frac{\partial I}{\partial n_k}\right)_{ss}\left[\left(\frac{d\alpha_k}{dv}\right)_{ss}-n_{k,\infty}\left(\frac{d(\alpha_k+\beta_k)}{dv}\right)_{ss}\right]\delta v \quad (9)$$

and $b_k=(\alpha_k+\beta_k)_{ss}$, where $n_{k,\infty}=\alpha_k/(\alpha_k+\beta_k)$ is the steady state. In order to understand Eq. (8), consider Fig. 2 and write the voltage of each inductance branch as

$$\delta v=\left(\frac{1}{g_k}+L_k\frac{d}{dt}\right)\delta I_k, \quad k=1,\ldots,M, \quad (10)$$

where δI_k is the current through both components g_k and L_k. It is similar to the second term on the right-hand side of Eq. (8). Indeed, the voltage δv across the electrical circuit with $M+1$ branches drawn in Fig. 2 is the same as δv in Eq. (8) if

$$g_k=\tau_k\left(\frac{\partial I}{\partial n_k}\right)_{ss}\left[\left(\frac{d\alpha_k}{dv}\right)_{ss}-n_{k,\infty}\left(\frac{d(\alpha_k+\beta_k)}{dv}\right)_{ss}\right], \quad (11)$$

where $\tau_k=1/(\alpha_k+\beta_k)$ and if we set inductances to

$$L_k=\frac{1}{g_k(\alpha_k+\beta_k)}=\frac{\tau_k}{g_k}, \quad k=1,\ldots,M. \quad (12)$$

Hence, for a small perturbation δv around the steady-state voltage v_{ss}, the current I responds as though the conductance G is in parallel with the M impedance lines. As in Fig. 2, each of these impedance lines are a conductance g_k in series with an inductance L_k.

From Eqs. (8) and (10), the linearized HH equations will be

$$c\frac{dv}{dt}=-\tilde{G}v-\sum_{k=1}^{M}I_k+I_{app}, \quad \tilde{G}=G+g_L, \quad (13)$$

$$L_k\frac{dI_k}{dt}=-\frac{I_k}{g_k}+v, \quad k=1,\ldots,M. \quad (14)$$

III. RESONATE-AND-FIRE NEURAL MODEL

The IF and the RF models are the simplest spiking neuron models that capture the essence of integrator and resonator neurons [27,36]. Their importance comes from the fact that they are computationally efficient and suitable for simulations of large networks of spiking neurons. A simple description of both models is that whenever voltage reaches the threshold potential, a spike is registered, the system state is instantly mapped to some reset value, and the dynamics continues.

The RF model is similar to the IF neuron model except that it can exhibit subthreshold resonance. That is the subthreshold membrane potential response of the neuron driven with a small oscillatory drive depends on the drive frequency and can be peaked at particular frequency [26]. This property that enables neurons to selectively respond to activities of other neurons is called *selective communication* [36].

The RF model is defined by functions that are piecewise smooth but event driven in the sense that smoothness is lost at instantaneous events, for example, upon application of the reset map. It has fascinating dynamics and a rich underlying mathematical structure. The RF system corresponds to the linearized HH Eqs. (13) and (14) with only one inductive path way. Therefore, the subthreshold behavior of the periodically forced RF system satisfies

$$c\frac{dv}{dt}=-\frac{v}{R}-I+I_{app}(t), \quad R=\frac{1}{\tilde{G}}, \quad r=\frac{1}{g},$$

$$L\frac{dI}{dt}=v-rI, \quad (15)$$

where v is the voltage, I is a resonant current, e.g., delayed rectifier K^+ or I_h, and $I_{app}(t)$ is periodic applied current such that $I_{app}(t+T)=I_{app}(t)$. The specific case we will study for our numerical simulations is $I_{app}(t)=I_0+\epsilon\sin(\omega_0 t)$, where ϵ is the amplitude of forcing, I_0 is a constant current, and ω_0 is the forcing frequency. It proves convenient to consider system (15) in the following form:

$$\dot{\mathbf{x}}=A\mathbf{x}+f(t), \quad (16)$$

where

$$A=\begin{pmatrix}-(Rc)^{-1} & -c^{-1}\\ L^{-1} & -rL^{-1}\end{pmatrix} \quad (17)$$

and

$$\mathbf{x}=\begin{pmatrix}v\\ I\end{pmatrix}, \quad f(t)=\begin{pmatrix}\frac{I_{app}(t)}{c}\\ 0\end{pmatrix}.$$

Let us assume the threshold potential can be defined by the zero set of a smooth function $h(\mathbf{x},t)=v-k(t)$,

$$\text{threshold} = \{\mathbf{x}(t): h(\mathbf{x}(t),t) = 0\}, \tag{18}$$

where $k(t)$ is a continuous function and in the simplest case can be constant. Therefore, the nth firing time t_n is defined as

$$t_n = \inf\{t | h(\mathbf{x}(t),t) \geq 0, t \geq t_{n-1}, v'(t) \neq k'(t)\},$$

where a prime denotes a derivative. Therefore, whenever the RF orbit intersects the threshold transversely, the instant transition from threshold takes place, which in fact changes the position of the RF orbit according to a reset map $\mathbf{R}$,

$$h(\mathbf{x},t) = 0: \quad \mathbf{x} \mapsto \mathbf{R}(\mathbf{x},t).$$

Suppose a spike occurs at time t_n. Let $\mathbf{x}^-$ and $\mathbf{x}^+$ represent the intersection of the RF flow with the threshold both immediately before and immediately after the crossing so that $\mathbf{x}^- = \lim_{t \to t_n^-} \mathbf{x}(t)$ and $\mathbf{x}^+ = \lim_{t \to t_n^+} \mathbf{x}(t)$. Hence, we can write the resetting mechanism of the trajectory at each firing time as

$$\mathbf{x}^+ = \mathbf{R}(\mathbf{x}^-,t). \tag{19}$$

The subthreshold behavior of the system (16) is linear and therefore easy to analyze. Its solution can be written as

$$\mathbf{x}(t) = G(t)\mathbf{x}(0) + \int_0^t G(t-s)f(s)ds, \tag{20}$$

where $G(t)$ is the matrix exponential (Green's function) $G(t) = \exp(At)$.

System (16) can show different types of subthreshold behavior associated with different neuronal characteristics. We are interested in resonant behavior and its corresponding region of parameters. In the parameter region where resonant behavior occurs, the system has either a stable node or a stable focus. As we want to focus on the occurrence of the mode-locked solutions and chaos, we do not describe different regimes here. For a complete classification of the subthreshold regime, see [26,28].

If the RF system has a stable focus, then matrix A has a complex-conjugate pair of eigenvalues $\alpha \mp i\omega$, with $\alpha = -(crR+L)/(2cRL)$ and $\omega^2 = (R+r)/(cRL) - \alpha^2$. For $\lambda = \alpha + i\omega$, the associated complex eigenvector is ν such that $\nu = \nu_R + i\nu_I \in \mathbb{C}^2$,

$$\nu = \begin{pmatrix} r + L\alpha \\ 1 \end{pmatrix} + i \begin{pmatrix} L\omega \\ 0 \end{pmatrix}.$$

In this case, $G(t) = e^{\alpha t} P R_\omega P^{-1}$, where

$$R_\omega = \begin{pmatrix} \cos(\omega t) & -\sin(\omega t) \\ \sin(\omega t) & \cos(\omega t) \end{pmatrix},$$

$$P = (\nu_I \quad \nu_R) = \begin{pmatrix} L\omega & r + L\alpha \\ 0 & 1 \end{pmatrix}.$$

Therefore, $G(t)$ has the explicit form

$$G(t) = \begin{pmatrix} G_{11}(t) & G_{12}(t) \\ G_{21}(t) & G_{22}(t) \end{pmatrix}, \tag{21}$$

with

$$G_{11}(t) = \frac{e^{\alpha t}}{L\omega}[L\omega \cos(\omega t) + (r + L\alpha)\sin(\omega t)], \tag{22}$$

$$G_{12}(t) = -\frac{e^{\alpha t}}{L\omega}[(L\omega)^2 + (r + L\alpha)^2]\sin(\omega t), \tag{23}$$

$$G_{21}(t) = \frac{e^{\alpha t}}{L\omega}\sin(\omega t), \tag{24}$$

$$G_{22}(t) = \frac{e^{\alpha t}}{L\omega}[L\omega \cos(\omega t) - (r + L\alpha)\sin(\omega t)]. \tag{25}$$

Similarly, in the case of a stable node, we have

$$G_{11}(t) = \frac{\exp(\lambda_1 t)(r + L\lambda_1) - \exp(\lambda_2 t)(r + L\lambda_2)}{L(\lambda_1 - \lambda_2)}, \tag{26}$$

$$G_{12}(t) = \frac{(r + L\lambda_1)(r + L\lambda_2)[\exp(\lambda_2 t) - \exp(\lambda_1 t)]}{L(\lambda_1 - \lambda_2)}, \tag{27}$$

$$G_{21}(t) = \frac{\exp(\lambda_1 t) - \exp(\lambda_2 t)}{L(\lambda_1 - \lambda_2)}, \tag{28}$$

$$G_{22}(t) = \frac{\exp(\lambda_2 t)(r + L\lambda_1) - \exp(\lambda_1 t)(r + L\lambda_2)}{L(\lambda_1 - \lambda_2)}, \tag{29}$$

where λ_1 and λ_2 are negative real eigenvalues of matrix A.

A. Firing time map

For simplicity, we assume that the RF oscillator is driven by a constant input I_0 so that in the absence of any periodic forcing it still oscillates. The RF system evolves smoothly between firing times so that we can define a discrete firing times map that expresses the system state at one firing time as a function of the state at the previous firing time. Using Eq. (20), we can write

$$\mathbf{x}(t_{n+1}) = G(\Delta^n)\mathbf{x}(t_n) + \int_0^{\Delta^n} G(s)f(-s + t_{n+1})ds, \tag{30}$$

where $\Delta^n = t_{n+1} - t_n$ is the interspike interval (ISI). Now we assume the simple case of the threshold function as

$$h(\mathbf{x},t) = v - 1 \tag{31}$$

and define the resetting mechanism by

$$\mathbf{x}^+ = \mathbf{R}(\mathbf{x}^-,t) = \mathbf{0}. \tag{32}$$

Substituting these conditions into Eq. (30) gives a one-dimensional time map in the implicit form

$$F(t_n, t_{n+1}) \equiv \int_0^{\Delta^n} G_{11}(s) I_{app}(-s + t_{n+1})ds - c = 0, \tag{33}$$

as well as an expression to evaluate the current at firing time t_{n+1},

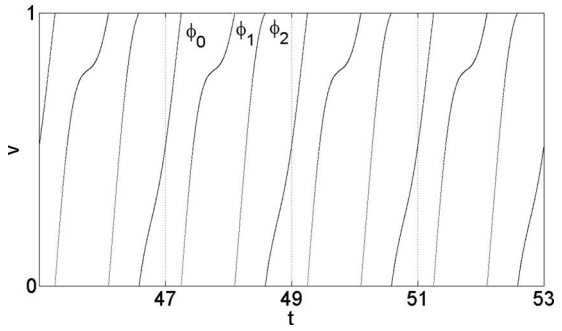

FIG. 3. An example of a 3:2 mode-locked solution showing the membrane voltage trajectory that may arise in a sinusoidally driven RF system given in Eqs. (16), (31), and (32) with $I_{app}=2.23+\sin(2\pi t)$, $R=c=L=1$, and $r=0.1$. Note that the system fires three spikes (with phases ϕ_0, ϕ_1, and ϕ_2) for every two periods of applied current.

$$I(t_{n+1}) = c^{-1}\int_0^{\Delta^n} G_{21}(s)I_{app}(-s+t_{n+1})ds. \tag{34}$$

Efficient numerical methods exist to compute the smooth flows, to determine the firing times, and to follow these as the system parameters vary. In the next section, we focus on mode-locked solutions.

B. Mode-locked solutions

To classify possible rhythms of the firing time of the RF system, we use the theory of mode locking, which relates the period of the output spike train to the period of forcing rationally. That means the RF orbit repeats exactly after a fixed number, p, of spikes and a fixed number, q, of forcing period T; the resulting train is called a $p:q$ mode-locked state. Therefore, the winding number of a $p:q$ mode-locked solution is $\frac{p}{q}$, that is, the average number of firing events per period of the forcing. We can construct mode-locked solutions explicitly and analyze how their existence changes as we vary a parameter.

It is convenient to introduce the nth firing time of a $p:q$ mode-locked solution as in [10,20] as

$$t_n = \left(\left[\frac{n}{p}\right] + \phi_{n(p)}\right)qT, \quad n = 0,1,2\ldots,$$

$$n(p) = n \bmod p, \tag{35}$$

where $\phi_0,\ldots,\phi_{p-1}\in[0,1)$ are a collection of firing phases, $[\cdot]$ denotes the integer part, and T is the period of applied current.

Figure 3 shows an example of 3:2 mode-locked state of the RF system represented by the voltage orbit for $I_{app}(t)=2.23+\sin(2\pi t)$. As one expects, within each two periods of the driving signal, three spikes are fired with corresponding phases ϕ_0, ϕ_1, and ϕ_2.

Substituting Eq. (35) into Eq. (33), we find that the p firing phases $(\phi_0,\ldots,\phi_{p-1})$ are determined by the p equations

$$F_n(\Phi,qT) \equiv \int_0^{\Delta^n} I_{app}(-s+\phi_{n+1(p)}qT)G_{11}(s)ds - c = 0, \tag{36}$$

where $\Phi=(\phi_0,\phi_1,\ldots,\phi_{p-1})$ and $n=0,\ldots,p-1$. However, not all of the values of Φ obtained by such a procedure actually correspond to a $p:q$ mode-locked solution. They must also satisfy conditions that guarantee that such an orbit is physically possible. From the definition of firing times and the resetting map, we already know that one such restriction is

$$\frac{dv}{dt}(t_n) \neq 0, \quad n = 0,\ldots,p-1.$$

As parameters in the system vary, this condition may be broken at certain isolated values, giving rise to *grazing bifurcation* points, at which the qualitative properties of the solution change, often in a dramatic manner. This kind of bifurcation, which is the result of crossing and resetting rules, is called a *discontinuity-induced-bifurcation* (DIB) and we address them later (for more details, see [29]). Therefore, in general, we can find the $p:q$ mode-locked solutions by simultaneously solving the p Eq. (36). Moreover, the average of the firing period is defined by $\langle\Delta\rangle=\lim_{N\to\infty}1/N\Sigma_{n=0}^{N}\Delta^n$. Therefore, using Eq. (35), the average of a $p:q$ mode-locked solution satisfies $\langle\Delta\rangle=\frac{q}{p}$. For periodically forced systems, there typically exist regions in parameters space in which mode-locked solutions exist. These regions are called *Arnol'd tongues*, emanating from rational points on the zero forcing ($\epsilon=0$) and opening up into regions where the forcing strength is turned on. Each tongue corresponds to a locked solution for which the ratio of the forcing frequency to the firing frequency is $\frac{q}{p}$ for $p,q\in\mathbb{Z}$. The boundaries of these tongues are determined by finding the conditions of instability of the relevant mode-locked orbit. By mapping out these boundaries, we can try to partition the parameter space in terms of the qualitative behavior of the system.

C. Stability

The structure of Arnol'd tongues can be affected by various bifurcations. We can classify them as smooth bifurcations of the firing map when mode-locked solutions lose their stability and nonsmooth bifurcations arising from the discontinuity of the system (DIBs). Here we aim to explain these bifurcations.

To detect smooth bifurcation, the stability of mode-locked solutions must be examined. Hence, similar to that in [10,20], we perturb the nth firing time about a mode-locked solution such that

$$t_n \to t_n + \delta_n = t_n^*.$$

The perturbation of firing map (33) is then expressed as

$$F(t_{n+1}^*,t_n^*) \equiv \int_0^{t_{n+1}^*-t_n^*} G_{11}(s)I_{app}(-s+t_{n+1}^*)ds - c = 0. \tag{37}$$

Retaining only the first-order term, we arrive at

$$\frac{\partial F}{\partial t_{n+1}}\delta_{n+1} + \frac{\partial F}{\partial t_n}\delta_n = 0, \tag{38}$$

where the partial derivatives are evaluated at the mode-locked solution. We can rewrite Eq. (38) as

$$\delta_{n+1} = \frac{\Gamma_n}{\Phi_n}\delta_n \equiv \kappa_n \delta_n, \tag{39}$$

where the coefficients are

$$\Gamma_n = -\frac{\partial F}{\partial t_n} = G_{11}(\Delta^n) I_{app}(t_n),$$

$$\Phi_n = \frac{\partial F}{\partial t_{n+1}} = \Gamma_n + \int_0^{\Delta^n} G_{11}(s)\frac{dI_{app}}{dt}(-s + t_{n+1})ds. \tag{40}$$

Therefore, the stability of a $p:q$ mode-locked state is determined by the behavior of the map

$$\delta_{n+1} = \kappa(p)\,\delta_{n+1-p}, \tag{41}$$

where

$$\kappa(p) = \kappa_0 \kappa_1 \cdots \kappa_{p-1}. \tag{42}$$

If $\ln|\kappa(p)| < 0$, the corresponding mode-locked solution is stable. Upon variation of a parameter, when $|\kappa(p)|$ passes through 1, some bifurcations occur. Specifically, we expect to observe tangent bifurcation when $\kappa(p)=1$ and period-doubling bifurcation when $\kappa(p)=-1$. Tangent bifurcation is not the only way in which the periodic orbits of the RF system can change their qualitative behavior as the parameters governing the system vary. Also, if periodic solutions have tangential intersections with the threshold curve, grazing bifurcation occurs [29] in which we see changes in behavior that are different from those of the smooth system. The linear stability analysis of the firing map will not detect such kinds of bifurcations (DIBs) that occur when mode-locked solutions interact with discontinuities of the firing map. In general, there could be two types of grazing bifurcations [20,29].

Type 1 grazing arises when varying a parameter in the RF system causes a local maximum to increase through the firing threshold, leading to a new firing event that occurs at some time earlier than usual and between two existing firing times [see Fig. 4(a)]. With this assumption, a type 1 nonsmooth bifurcation is defined by

$$v(t_{new}) = 1, \quad t_n < t_{new} < t_{n+1}, \tag{43}$$

$$\frac{dv}{dt}(t_{new}) = 0, \tag{44}$$

where at t_{new}, a tangential crossing with the threshold function occurs and t_{n+1} is the appropriate solution of $F(t_n, t_{n+1}) = 0$. For $p:q$ mode-locked solutions, to find the graze phase and p firing phases, we need to solve $p+2$ nonlinear algebraic equations. These are the p equations (36) defining the mode-locked solutions with the extra two being Eqs. (43) and (44). Equations (43) and (44) can be written as

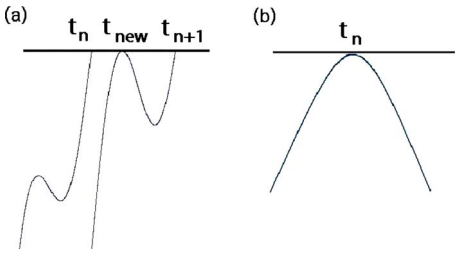

FIG. 4. (Color online) Grazing bifurcations whenever a tangential crossing of the firing threshold occurs. (a) A local maximum increases through the firing threshold and creates a new firing time. (b) A local maximum decreases through the threshold, causing the solution to be lost in a nonsmooth bifurcation [20].

$$\int_0^{t_{new}-t_n} G_{11}(s) I_{app}(-s + t_{new})ds - c = 0,$$

$$\int_0^{t_{new}-t_n} G_{11}(s)\frac{dI_{app}}{dt}(-s + t_{new})ds + G_{11}(t_{new} - t_n) I_{app}(t_n) = 0. \tag{45}$$

Note that for this kind of nonsmooth bifurcation, we should specify between which two existing firing times the graze occurs. Therefore, for small changes in parameters, it is then possible to have $p+1:q$ mode-locked solution from $p:q$ solution.

In Fig. 5, we exhibit the analytical Arnol'd tongues structure. The boundaries of Arnol'd tongues are determined by both tangent bifurcations (solid lines) and type 1 grazing bifurcations (dashed lines). As we see, unlike the case of the smooth circle map [37,38], the tongues do not intersect each other anymore. Figure 5 also illustrates another feature of the Arnol'd tongues, namely, those emanating from the zero forcing amplitude are arranged such that between the $p:q$ and the $p':q'$ tongues, one can expect to see the $p+p':q+q'$ tongue, e.g., between 3:2 and 2:1, the 5:3 tongue, between 2:1 and 3:1, the 5:2 tongue, and between 1:1 and 3:2, the 4:3 tongue can be seen. This concatenation of the peri-

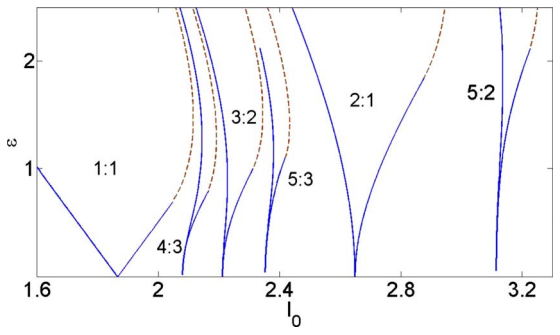

FIG. 5. (Color online) Boundaries of 1:1, 4:3, 3:2, 5:3, 2:1, and 5:2 tongues, constructed from the union of smooth bifurcations of the firing map and nonsmooth bifurcations induced by discontinuity of the system. Solid lines indicate a tangent bifurcation of the firing map and dashed lines a nonsmooth grazing bifurcation of the underlying flow. Parameters are as in the caption of Fig. 3.

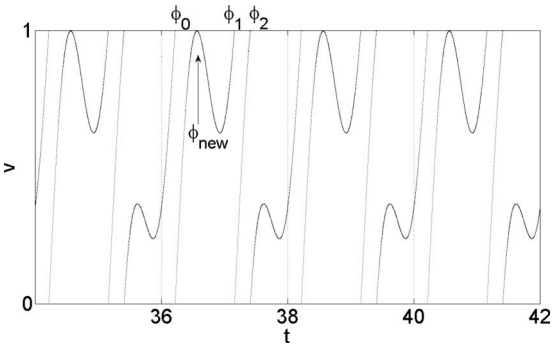

FIG. 6. Voltage trajectory of the RF system for the parameter values $I_0=2.27$ and $\epsilon=2.65$ on the graze locus of the 3:2 tongue shown in Fig. 5. Other parameters are as in Fig. 3. The voltage orbit crosses the threshold at phases ϕ_0, ϕ_1, and ϕ_2 transversely and, as we expect, it tangentially touches threshold between ϕ_0 and ϕ_1 at a new phase ϕ_{new}.

odic orbits shows a striking resemblance with the well-known series in number theory proposed by Farey and this phenomenon is referred as Farey arithmetic. It has been shown in [29] that periodic orbits of one-dimensional discontinuous piecewise linear map exhibit the same interesting relationship between nearby periodic orbits.

We can also verify the occurrence of the graze by looking at the voltage trajectory on the graze locus. This is shown in Fig. 6 for $I_0=2.27$ and $\epsilon=2.65$ where one expects to see three spikes, namely, ϕ_0, ϕ_1, and ϕ_2, within every two periods of $I_{app}(t)$. Moreover, it is clear that the graze as a local maximum arrives between ϕ_0 and ϕ_1 while touching the threshold surface tangentially. This is a bifurcation point for the creation of a new firing time where the 3:2 mode-locked solution turns into the 4:2 mode-locked solution.

The method to exhibit a $p:q$ Arnol'd tongue in the (I_0,ϵ)-parameter plane is to find a p-periodic point on the tangent-bifurcation curve. It can be done by simultaneously solving p equations (36) which satisfy $\kappa(p)=1$. Continuation of this solution on the tangent-bifurcation locus in the ϵ and I_0 plane constructs part of the boundary of the tongue. The continuations of Arnol'd tongues are one-parameter continuations in two-parameter space. For a complete discussion on the computing of Arnol'd tongues, see [39] and for discussion on the smooth circle map, its bifurcations, and the corresponding Arnol'd tongues, see [37,38].

Grazing of type 2 also occurs whenever varying a parameter causes the voltage to reach the threshold but with $\frac{dv}{dt}=0$ at that time, rather than $\frac{dv}{dt}>0$ [see Fig. 4(b)]. This may also cause the solution to be lost in a nonsmooth bifurcation [10,29] where for small variation of parameters, the $p:q$ mode-locked state turns into the $p-1:q$ mode-locked state. This bifurcation could be detected by appending the condition $\frac{dv}{dt}(t_n)=0$ to the p equations (36) defining the mode-locked orbit. Care must be taken to determine at which firing time the graze takes place.

Therefore, considering both smooth bifurcations of the firing map and the grazing bifurcations of the underlying discontinuous flow, we were able to construct the Arnol'd tongue structure of the periodically driven RF system. In the determination of the tongues, period-doubling bifurcation does not occur and type 2 grazing bifurcation does not seem to play a large role, although is present.

Whenever the grazing bifurcations occur, the map of firing times becomes discontinuous. This discontinuity situation close to a grazing point is due to the fact that a trajectory starting close to the graze either intersects the threshold with small value of $\frac{dv}{dt}$ or does not intersect the threshold locally. This causes a drastic difference in subsequent behavior of the trajectories close to the graze.

Using Eq. (39), the derivative of the firing times map is obtained as

$$\frac{\partial t_{n+1}}{\partial t_n}=\frac{\Gamma_n}{\Phi_n} \tag{46}$$

and it becomes unbounded whenever $\Phi_n=0$. In both types of the grazing bifurcations, the derivative of the map becomes unbounded and the map of firing times is discontinuous. For example, in the case of 1:1 mode-locked solutions, using the fact that $t_{n+1}-t_n=T$ and $t_n=nT+\phi_0$, the discontinuity condition for the firing map reads

$$G_{11}(T)I_{app}(\phi_0)+\int_0^T G_{11}(s)\frac{dI_{app}}{dt}(-s+\phi_0)ds=0,$$

which is satisfied if

$$\int_0^T \frac{d}{dt}G_{11}(s)I_{app}(-s+\phi_0)ds+I_0<\epsilon. \tag{47}$$

In general, it is complicated to determine the parameter regions in which $\Phi_n=0$, but as illustrated in the analytical Arnol'd tongue structure, for a $p:q$ mode-locked solution, the firing map is discontinuous on the locus of the graze. This is shown with dashed lines on Fig. 5.

If the RF firing map is continuous, it is only invertible if $\Gamma_n\neq 0$. In this case, from the firing map (33), we know that if $F(t,s)=0$, then $F(t+T,s+nT)=0$ for $n=1$, indicating that F is the lift associated to a degree one circle map. Therefore, the firing map is an invertible circle map when $I_{app}(t_n)\neq 0$ and $G_{11}(\Delta^n)\neq 0$.

It is straightforward to see that $I_{app}(t_n)\neq 0$ when $I_0>\epsilon$. Given that the RF system has stable node and using Eq. (26), the condition $G_{11}(\Delta^n)\neq 0$ is satisfied and for the RF system with stable focus, using Eq. (22), this condition translates into

$$\frac{L\omega}{r+L\alpha}\neq -\tan(\omega\Delta^n).$$

Therefore in the region of 1:1 mode-locked solutions, the firing map is invertible circle map if

$$\int_0^T \frac{d}{dt}G_{11}(s)I_{app}(-s+\phi_0)ds\geq 0, \tag{48}$$

and if the RF system has stable focus, both conditions (48) and $L\omega/(r+L\alpha)\neq -\tan(\omega T)$ must satisfy.

The map of firing times is not necessarily onto. To ensure that the firing map is onto, the slope of the voltage at the firing times must be larger than the slope of the threshold, that is $\frac{d}{dt}v(t_n) > 0$.

Now using a dynamical-systems approach, we investigate the dynamics of the RF model in terms of chaotic behavior. This is achieved by calculation of *Liapunov exponents*. If the largest Liapunov exponents is positive, the system is recognized as chaotic. We need to use the idea originally developed for the study of impact oscillators [32] to calculate the largest Liapunov exponents. This idea has been also used for calculation of the Liapunov exponents of the IF model [40] and IF model with threshold fatigue [15]. For completeness and subsequent conclusion, in the next section, we focus on the notion of Liapunov exponents for the RF system.

IV. LIAPUNOV EXPONENTS

For our purpose which is to determine the existence of chaos, we establish that there are regions in parameter space in which the RF model displays sensitive dependence on initial conditions as indicated by positive Liapunov exponent. To this end, we calculate an expression for the Liapunov exponents of the RF model given in Eq. (16).

Liapunov exponents of the RF model can be derived by determining the slopes of the firing map at successive firing times. While the subthreshold dynamics of the RF system is continuous, the effect of the flow reaching threshold is to cause an instantaneous jump in the flow and introduces a nonlinearity into the dynamics. Therefore, the standard approach of calculation of Liapunov exponents is not applicable for the RF model. Instead, we use the ideas developed for the study of impact oscillators [32] to estimate Liapunov exponents. The main step in this method is to evaluate the consequence of these discontinuities on solutions starting from nearby initial conditions.

Consider the RF system (16) with threshold and resetting conditions given in Eqs. (31) and (32). Let us assume there is a small perturbation $\delta\mathbf{x}(t_0)=[\delta v(t_0), \delta I(t_0)]^T$ (where the superscript T denotes vector transposition) on an initial condition $\mathbf{x}(t_0)=[v(t_0), I(t_0)]^T$. In the absence of firing in the interval $[0,t]$, the initial perturbation evolves to the value

$$\delta\mathbf{x}(t) = \begin{pmatrix} \delta v(t) \\ \delta I(t) \end{pmatrix} = G(t)\,\delta\mathbf{x}(t_0),$$

where $G(t)$ is given in Eq. (21). To calculate the Liapunov exponents, we follow the temporal generation of this perturbation and trace it immediately before the unperturbed orbit crosses the threshold, denoted by $\delta\mathbf{x}^-$ and immediately after the perturbed orbit crosses the threshold, denoted by $\delta\mathbf{x}^+$. We assume the unperturbed solution reaches threshold before the perturbed one at time t_1, then we have

$$\delta\mathbf{x}(t) = G(t-t_1)B(t_1)G(t_1-t_0)\,\delta\mathbf{x}(t_0), \tag{49}$$

where matrix B is related to the derivation of $\delta\mathbf{x}^+$ and is calculated as below.

Let us assume the perturbed solution, $\tilde{\mathbf{x}}(t)$, intersects threshold at time $t_1+\delta t_1$. The situation is illustrated in Fig. 7.

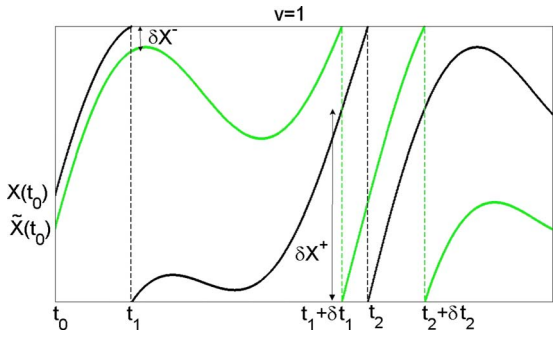

FIG. 7. (Color online) Illustration of the method for calculating the Liapunov exponents of the RF model given in Eqs. (16), (31), and (32). The unperturbed solution $\mathbf{x}(t)$ intersects the threshold at times t_n while the perturbed solution $\tilde{\mathbf{x}}(t)$ intersects at time $t_n+\delta t_n$. In order to calculate Liapunov exponents, we trace $\delta\mathbf{x}^+ = \tilde{\mathbf{x}}(t_n+\delta t_n^+) - \mathbf{x}(t_n+\delta t_n^+)$ as explained in the text.

The goal is to derive an expression for $\delta\mathbf{x}^+ = \delta\mathbf{x}(t_1+\delta t_1^+)$ as a function of $\delta\mathbf{x}^- = \delta\mathbf{x}(t_1^-)$, keeping only first-order terms.

Using the crossing condition (31) and the fact that $\tilde{\mathbf{x}}(t) = [\tilde{v}(t), \tilde{I}(t)]^T$, $\delta v(t) = \tilde{v}(t) - v(t)$, and $\delta I(t) = \tilde{I}(t) - I(t)$, at time $t_1+\delta t_1$, we have

$$0 = h(\tilde{\mathbf{x}}(t_1+\delta t_1)) = \tilde{v}(t_1+\delta t_1) - 1 \approx \tilde{v}(t_1) + \delta t_1 \tilde{v}'(t_1) - 1$$
$$\approx \delta v(t_1) + \delta t_1 v'(t_1), \tag{50}$$

where a prime denotes a derivative. Therefore, the perturbation of firing time t_1 is approximately given by

$$\delta t_1 = \frac{-\delta v(t_1)}{v'(t_1)}, \tag{51}$$

where we have assumed the denominator is not zero. At $t = t_1+\delta t_1^+$, using the resetting condition (32), we have

$$\delta v^+ = \delta v(t_1+\delta t_1^+) = \tilde{v}(t_1+\delta t_1^+) - v(t_1+\delta t_1^+) \approx -\delta t_1 v'(t_1^+). \tag{52}$$

Furthermore, we have

$$\delta I^+ = \tilde{I}(t_1+\delta t_1^+) - I(t_1+\delta t_1^+) \approx -I(t_1^+) - \delta t_1 I'(t_1^+) = 0. \tag{53}$$

Equations (51)–(53) result in

$$\delta v^+ = \alpha(t_1)\,\delta v(t_1), \quad \delta I^+ = 0,$$

where

$$\alpha(t) = \frac{I_{app}(t)}{I_{app}(t) - R^{-1} - I(t)}. \tag{54}$$

In this way, we have

$$B(t) = \begin{pmatrix} \alpha(t) & 0 \\ 0 & 0 \end{pmatrix}.$$

Now for the general case where there are n spikes at times $0 \le t_1 < \cdots < t_n < t$, we get

$$\delta\mathbf{x}(t) = G(t-t_n)B(t_n)G(t_n-t_{n-1}) \cdots G(t_2-t_1)B(t_1)G(t_1-t_0)\delta\mathbf{x}(t_0). \quad (55)$$

The Liapunov exponents measure the average rate of expansion or compression of this quantity and are defined as

$$\lambda = \lim_{t\to\infty}\frac{1}{t}\ln\left(\frac{|\delta\mathbf{x}(t)|}{|\delta\mathbf{x}(t_0)|}\right).$$

It proves convenient to estimate the Liapunov exponents by starting and ending the computation at firing times, therefore using Eq. (55) and the definition of matrix B, we have

$$\delta\mathbf{x}(t_n) = M_n\delta\mathbf{x}(t_0),$$

where

$$M_n = \begin{pmatrix} M_{n,1} & 0 \\ 0 & 0 \end{pmatrix},$$

with

$$M_{n,1} = \prod_{i=1}^{n}\alpha(t_i)G_{11}(t_i - t_{i-1}). \quad (56)$$

Then the two Liapunov exponents can be defined from the eigenvalues of matrix $L_n = M_n M_n^T$. If λ_n is an eigenvalue of L_n, the corresponding Liapunov exponent, λ, is defined by

$$\lambda = \lim_{n\to\infty}\frac{1}{2n}\ln(\lambda_n). \quad (57)$$

One of the eigenvalues of the matrix L_n is zero resulting the Liapunov exponent μ such that $\mu\to-\infty$. Calculating the other eigenvalue and using Eqs. (54), (56), and (57), we have the largest Liapunov exponent of the RF model as

$$\lambda = \lim_{n\to\infty}\frac{1}{t_n}\ln\prod_{i=1}^{n}|\alpha(t_i)G_{11}(\Delta^{i-1})|. \quad (58)$$

In the cases of the stable focus and the stable node of the RF model, it is easy to see from Eqs. (22) and (26) that two factors contribute to the Liapunov exponent λ: one from the smooth flow between successive firing events and the other from the discontinuity induced by the resetting. Figures 8(a) and 10 show the Liapunov exponent (color coded) associated with Eq. (58). At each point in the parameter plane, the Liapunov exponent is approximated over 3000 firing times and the first 100 firing times were ignored as transients. Figure 8(a) shows the Liapunov exponent as a function of I_0 and ϵ for $\omega_0=2\pi$. Other parameters are as in the caption of Fig. 3. When $\epsilon=0$, i.e., there is no temporal modulation of the input current, the model displays periodic or quasiperiodic behavior ($\lambda\leq 0$). We observe the Arnol'd tongues emanating from the ϵ axis (compare to Fig. 5), the largest being the 1:1 tongue. As we see, the model does not show chaotic behavior. Figure 8(b) shows a winding number diagram corresponding to the Arnol'd tongue structure in Fig. 8(a) for $\epsilon=1$. Every step on the devil's staircase is associated with a rational value of $\langle\Delta\rangle^{-1}$. As can be seen from devil's staircase, the winding number in locking regions follows the Farey sequence. For $\epsilon=1$, we also exhibit the bifurcation diagram

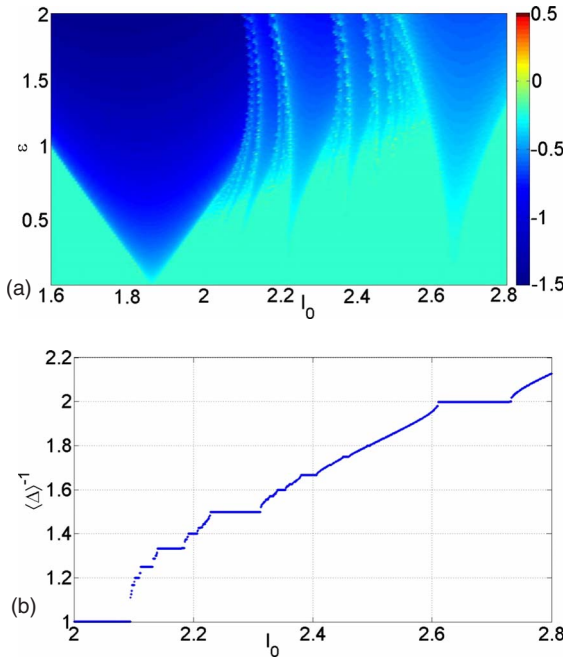

FIG. 8. (Color online) (a) The Liapunov exponent as a function of I_0 and ϵ for $\omega_0=2\pi$ on a mesh of size 300×300 corresponds with the bifurcation diagram in Fig. 5 and (b) the average of the firing frequency of the RF model as a function of I_0 with constant $\epsilon=1$. Note that the dominant mode-locked solutions are 1:1, 4:3, 3:2, and 2:1 (with increasing I_0). Other parameters are as in the caption of Fig. 3.

of the interspike interval $\Delta^n=t_{n+1}-t_n$ as a function of I_0 in Fig. 9(a) and its corresponding Liapunov exponent for the same range of I_0 in Fig. 9(b). We see that the Liapunov exponent is either negative or zero so no chaotic behavior is observed. In Fig. 9(a), we observe periodic solutions at different values of I_0, for example, while increasing I_0, we have period-1, period-4, period-3, period-5, and period-2 solutions indicated by labels in the figure. As expected, their corresponding regions in Fig. 9(b) exhibit negative Liapunov exponent. In Fig. 10, we show the Liapunov exponent as a function of the forcing frequency, ω_0, and ϵ for $I_0=2.45$. As seen in Fig. 8(a), when $I_0=2.45$, the system does not show chaotic behavior, however in Fig. 10 (color coded), we observe that increasing the forcing amplitude can move the system from periodic to chaotic behavior as ω_0 increases and passes through the resonant frequency at approximately 1.2. For $\epsilon=1.02$, Fig. 11(a) represents the impact of varying ω_0 on the interspike interval bifurcation diagram, while Fig. 11(b) shows the RF Lispunov exponent λ for the same range of ω_0. In the regions of periodic solutions, as expected, we observe negative Liapunov exponent. Some intervals of values of ω_0 for which periodic orbit exists are indicated with labels in Fig. 11(a). However, as ω_0 is decreased, we see windows of periodic solutions alternating with windows of chaotic dynamics. Besides the existence of chaos, Fig. 11(a) gives valuable information about the transitions leading to chaos. It reveals the phenomenon of *period adding* [29] leading to chaos. As ω_0 is decreased, we see periodic solutions such that their period increases in an arithmetic sequence. In this situation, either between periodic solutions of period n

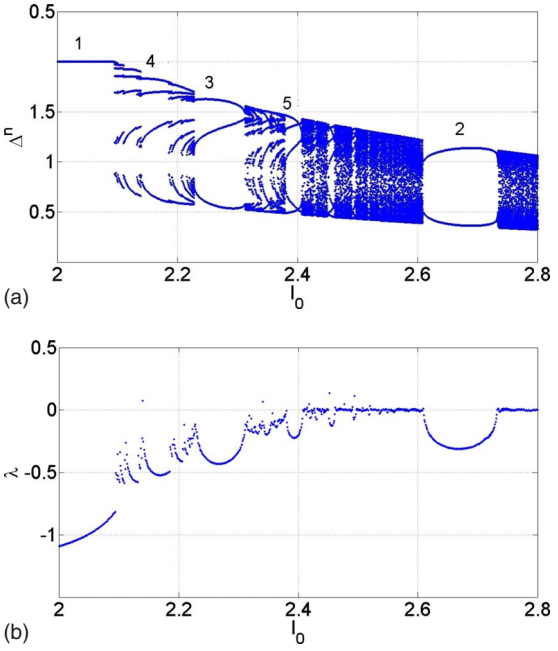

FIG. 9. (Color online) For constant $\epsilon=1$ in Fig. 8(a), we represent (a) the bifurcation diagram for ISI. The lines in the bifurcation diagram correspond to periodic solutions. Some periodic regions are indicated with labels showing their period. (b) The corresponding Liapunov exponent, as we see, λ is either negative or zero. We used 1000 firing times to estimate λ at each value of I_0. Other parameters are as in the caption of Fig. 3.

and $n+1$, we observe an interval of ω_0 for which chaotic dynamics occurs or no chaotic behavior occurs and periodic solutions overlap for small intervals of ω_0. A similar dynamics is observed in square-root map arising as local approximation to the Poincaré maps associated with grazing bifurcations in impacting systems [29]. We discuss this behavior below.

In Fig. 12, we show an enlarged section of Fig. 11(a) in the range $\omega_0=1.55$ to $\omega_0=2.5$. At $\omega_0=2.5$, there is a period-4 solution. Upon decreasing ω_0, the period-4 orbit undergoes period doubling at $\omega_0\approx 2.24$ and thereafter the orbit evolves to period-5 orbit at $\omega_0\approx 2.19$. Between period-4 and period-5 intervals, there is a small interval of ω_0 where the periodic solutions overlap.

Decreasing ω_0, the period-5 orbit doubles at $\omega_0\approx 1.94$ and the orbit then passes through the discontinuities at ω_0

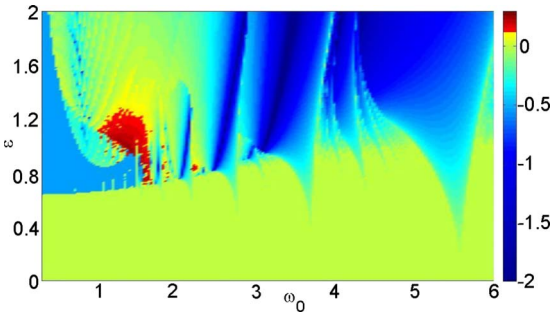

FIG. 10. (Color online) The Liapunov exponent of the RF model given in Eq. (58) as a function of ϵ and ω_0 with $I_0=2.45$. Other parameters are as in the caption of Fig. 3.

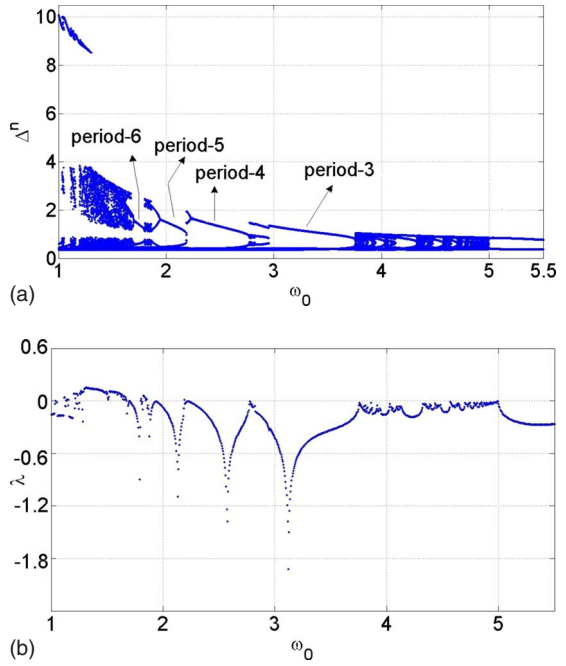

FIG. 11. (Color online) Bifurcation diagrams for fixed $\epsilon=1.02$ and $I_0=2.45$ in Fig. 10. In parts (a) and (b), we exhibit the bifurcation diagram of the interspike interval and the Liapunov exponent, respectively, as a function of forcing frequency. These are in good agreement. As one expects, regions with $\lambda<0$ in (b) correspond to periodic solutions in (a). For ω_0 near to the resonant frequency $1.2<\omega_0<1.6$, we observe chaotic behavior corresponding to $\lambda>0$.

≈ 1.93, $\omega_0\approx 1.92$, and $\omega_0\approx 1.85$, where we see the intersections in the interspike interval diagram (shown with the circles in Fig. 12). At these points, the orbit crosses threshold tangentially, corresponding to the discontinuities of the firing map.

The dynamics within the range of $1.8<\omega_0<1.86$ becomes chaotic. As ω_0 is lowered from 1.8, period-6 orbit appears. Then the orbit doubles at $\omega_0\approx 1.7$, giving rise to a chaotic interval in the range $1.3<\omega_0<1.67$.

In Fig. 13, we show ISI bifurcation diagram for $0.8<\omega_0<1.3$. We observe alternating windows of periodic solutions and chaotic motions, as ω_0 is decreased from 1.3 to 1.

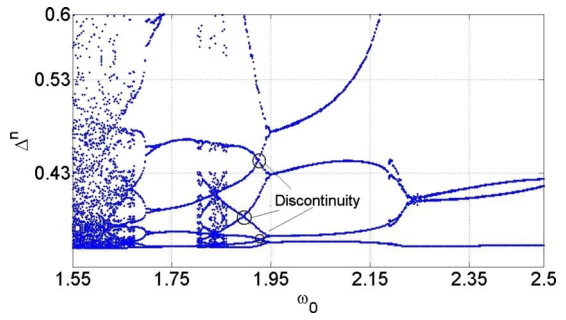

FIG. 12. (Color online) Enlargement of the bifurcation diagram shown in Fig. 11(a) in the range $\omega_0=1.55$ to $\omega_0=2.5$, showing transition to chaos. The circles are indicating the discontinuity points of the firing map.

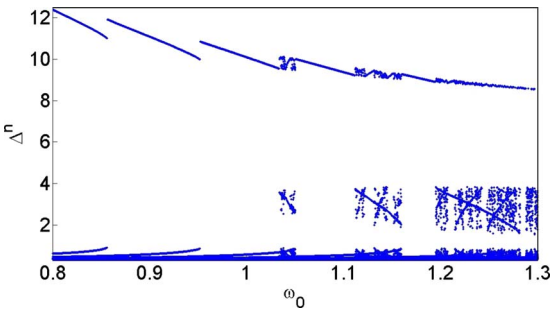

FIG. 13. (Color online) The bifurcation diagram in the range $\omega_0=0.8$ to $\omega_0=1.3$, showing period-adding phenomenon.

Thereafter, decreasing ω_0 in the range $\omega_0=1$ to $\omega_0=0.8$, we have period-adding scenario without chaotic intervals. At $\omega_0=1$, we see period-7 orbit which evolves smoothly to period 8 at $\omega_0\approx 0.95$, then the period-8 orbit gives rise to a period-9 orbit at $\omega_0=0.85$. Note that there is overlapping between these periodic orbits for small range of ω_0.

A useful way of studying one-dimensional map is via cobweb diagrams which plot t_{n+1} against t_n. An example of cobweb diagrams for the RF firing map is given in Fig. 14. As we see by varying parameters, the system may have (a) chaotic, (b) quasiperiodic, or [(c) and (d)] periodic behavior (showing, respectively, period-3 and period-5 orbits).

In the limit of large r, one expects that the RF model can be reduced to the IF model. To verify this, let us take $r=800$, $L=0.01$, and $c=1$ with forcing frequency $\omega_0=2\pi$ and the constant current $I_0=2$. For the sake of consistency with the results of Arnol'd tongues for the IF system [10,41], we show the bifurcation diagram in (ϵ,R) plane. The result is given in Fig. 15. Here, solid lines and dashed lines demonstrate tangent and grazing bifurcations, respectively. This is in good agreement with the results shown in [41].

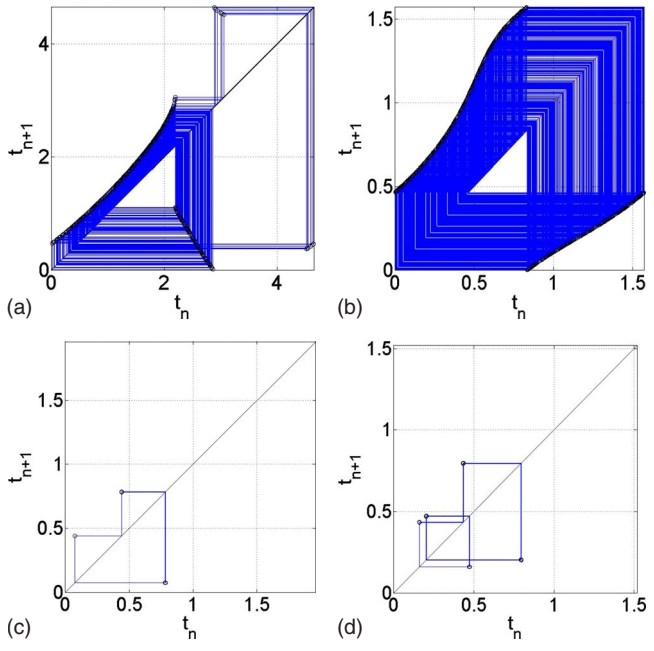

FIG. 14. (Color online) Cobweb diagrams for the firing map (33) showing (a) chaotic behavior, (b) quasiperiodic behavior, (c) period-3 attractor, and (d) period-5 attractor. Other parameters are as in Fig. 3.

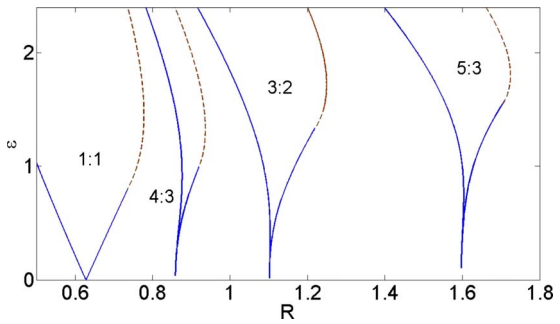

FIG. 15. (Color online) The Arnol'd tongues of the RF system in the limit of large r is compatible with those of the IF system shown in [41]. The forcing frequency is $\omega_0=2\pi$, the constant current is $I_0=2$, and the other parameters are $r=800$, $L=0.01$, and $c=1$. The boundaries of the tongues are determined by both tangent bifurcations (solid lines) and grazing bifurcations (dashed lines).

V. DISCUSSION

We have exactly analyzed the response of the RF neuron model to an arbitrary periodic modulation of its input current. The focus was on the occurrence of the mode-locked solutions and chaotic behavior. We have found that the analytically calculated regions of stability of mode-locked solutions, the Arnol'd tongues, are in excellent agreement with those of the numerical integration of the model [compare Figs. 5 and 8(a)]. The behavior of the system when periodically forced can be largely understood by tracing boundaries of the Arnol'd tongues. The boundaries of these tongues correspond to either local bifurcations of the firing time map or grazing bifurcations induced by the discontinuity of the flow. We showed that the behavior of the RF system can become chaotic when the forcing frequency is close to the resonant frequency. This is an important result as it was shown that the periodically driven leakage integrate-and-fire oscillators fail to reproduce chaotic behavior [10], whereas this form of behavior has been observed experimentally. Although it is known that some modified IF neuron models subjected to periodic forcing such as the ghostbursting model [20] and IF with threshold fatigue [15] can exhibit chaotic behavior, they cannot describe resonant behavior and are not suitable for modeling resonant neurons. Furthermore, the RF model can be reduced (by choosing a large r) to the leaky IF neuron model and in this case, there is good agreement between the result (see Fig. 15). Therefore, the analysis of the periodically forced RF model is a good extension of previous works related to mode-locked solutions of the IF models. On the other hand, it was shown in [26,28] that a sufficient amount of noise was necessary for the subthreshold resonance to cause a firing rate resonance. Our results highlight that even in response to the nonnoisy periodic inputs, the subthreshold resonance generates chaotic firing events.

As the RF model is the simplest neuron model reproducing resonant behavior, it is suitable for further mathematical analysis of network phenomena involving resonant neurons.

It is certainly of great interest to understand the effect of noise on the firing events, mode-locked solutions, and the structure of Arnol'd tongues of the RF system. Also considering the resetting map to reset just voltage obtains a two-dimensional firing map. In this case, it is worth understanding the properties of the firing times and the dynamics in terms of chaotic or periodic behavior. For two strongly coupled RF models, the synchronization state and the effect of the resetting function have been studied in [42]. Another interesting issue we would like to address is to analyze the response of a weakly connected population of firing RF neurons. One may then investigate the underlying conditions for synchronization or desynchronization states.

ACKNOWLEDGMENTS

The author would like to thank Claude Baesens, Stephen Coombes, and Yulia Timofeeva for many useful discussions. The author is supported by the University of Warwick.

[1] B. Hutcheon, R. M. Miura, Y. Yarom, and E. Puil, J. Neurophysiol. **71**, 583 (1994).
[2] E. Puil, H. Meiri, and Y. Yarom, J. Physiol. **71**, 575 (1994).
[3] Y. Gutfreund, Y. Yarom, and I. Segev, J. Physiol. (London) **483**, 621 (1995).
[4] B. Hutcheon, R. M. Miura, and E. Puil, J. Neurophysiol. **76**, 683 (1996); **26**, 698 (1996).
[5] H. Jahnsen and S. Karnup, Brain Res. **666**, 9 (1994).
[6] L. S. Leung and H. W. Yu, J. Neurophysiol. **79**, 1592 (1998).
[7] F. G. Pike, R. S. Goddard, J. M. Suckling, P. Ganter, N. Kasthuri, and O. Paulsen, J. Physiol. **529**, 205 (2000).
[8] C. Koch, *Biophysics of Computation* (Oxford University Press, Oxford, 1999).
[9] B. Hutcheon and Y. Yarom, Trends Neurosci. **23**, 216 (2000).
[10] S. Coombes and P. C. Bressloff, Phys. Rev. E **60**, 2086 (1999).
[11] F. Rieke, D. Warland, R. de Ruyter van Steveninck, and W. Bialek,*Exploring the Neural Code* (MIT Press, Cambridge, MA, 1997).
[12] A. S. French, A. V. Holden, and R. B. Stein, Kybernetik **11**, 15 (1972).
[13] J. F. Vibert and J. P. Segundo, Biol. Cybern. **33**, 81 (1979).
[14] M. Bezzi, T. Nieus, O. J. M. D. Coenen, and E. D'Angelo, Neurocomputing **58-60**, 593 (2004).
[15] M. J. Chacron, A. Longtin, and K. Pakdaman, Physica D **192**, 138 (2004).
[16] S. Coombes, M. R. Owen, and G. D. Smith, Phys. Rev. E **64**, 041914 (2001).
[17] D. T. Kaplan, J. R. Clay, T. Manning, L. Glass, M. R. Guevara, and A. Shrier, Phys. Rev. Lett. **76**, 4074 (1996).
[18] J. P. Keener, F. C. Hppensteadt, and J. Rinzel, SIAM J. Appl. Math. **41**, 503 (1981).
[19] K. K. Lin, SIAM J. Appl. Dyn. Syst. **5**, 179 (2006).
[20] C. R. Laing and S. Coombes, Int. J. Bifurcat. Chaos Appl. Sci. Eng. **15**, 1433 (2005).
[21] K. Yoshino, T. Nomura, K. Pakdaman, and S. Sato, Phys. Rev. E **59**, 956 (1999).
[22] C. Ascoli, M. Barbi, S. Chillemi, and D. Petracchi, Biophys. J. **19**, 219 (1977).
[23] A. Rescigno, R. B. Stein, R. L. Purple, and R. E. Poppele, Bull. Math. Biophys. **32**, 337 (1970).
[24] R. B. Stein, A. S. French, and A. V. Holden, Biophys. J. **12**, 295 (1972).
[25] R. R. Llinas, A. A. Grace, and Y. Yaromange, Proc. Natl. Acad. Sci. U.S.A. **88**, 897 (1991).
[26] N. Brunel, V. Hakim, and M. J. E. Richardson, Phys. Rev. E **67**, 051916 (2003).
[27] E. Izhikevich, Neural Networks **14**, 883 (2001).
[28] M. J. E. Richardson, N. Brunel, and V. Hakim, J. Neurophysiol. **89**, 2538 (2003).
[29] M. di Bernardo, C. J. Budd, A. R. Champneys, and P. Kowalczyk, *Piecewise-Smooth Dynamical Systems, Theory and Applications* (Springer, New York, 2008).
[30] K. Aihara, G. Matsumoto, and Y. Ikegaya, J. Theor. Biol. **109**, 249 (1984).
[31] H. Hayashi, S. Ishizuka, M. Ohta, and K. Hirakawa, Phys. Lett. A **88**, 435 (1982).
[32] P. C. Müller, Chaos, Solitons Fractals **5**, 1671 (1995).
[33] K. S. Cole, J. Gen. Physiol. **25**, 29 (1941).
[34] K. S. Cole, R. Guttman, and F. Bezanilia, Proc. Natl. Acad. Sci. U.S.A. **65**, 884 (1970).
[35] C. Koch, Biol. Cybern. **50**, 15 (1984).
[36] E. Izhikevich, Biosystems **67**, 95 (2002).
[37] P. L. Boyland, Commun. Math. Phys. **106**, 353 (1986).
[38] R. S. Mackay and C. Tresser, Physica D **19**, 206 (1986).
[39] F. Schilder and B. B. Peckam, J. Comput. Phys. **220**, 932 (2007).
[40] S. Coombes, Phys. Lett. A **255**, 49 (1999).
[41] S. Coombes and P. C. Bressloff, Phys. Rev. E **63**, 059901(E) (2001).
[42] K. Nakada, K. Miura, and H. Hayashi, Int. J. Bifurcat. Chaos Appl. Sci. Eng. **18**, 1249 (2008).